PvdL Orchestrates the Assembly of the Nonribosomal Peptide Synthetases Involved in Pyoverdine Biosynthesis in Pseudomonas aeruginosa

Hanna Manko, Tania Steffan, Véronique Gasser, Yves Mély, Isabelle Schalk, Julien Godet

International Journal of
Molecular Sciences

MDPI

Article

PvdL Orchestrates the Assembly of the Nonribosomal Peptide Synthetases Involved in Pyoverdine Biosynthesis in *Pseudomonas aeruginosa*

Hanna Manko [1,†], Tania Steffan [1], Véronique Gasser [2], Yves Mély [1,3], Isabelle Schalk [2] and Julien Godet [3,4,5,*]

[1] Laboratoire de BioImagerie et Pathologies, UMR CNRS 7021, ITI InnoVec, Université de Strasbourg, 67401 Illkirch, France
[2] CNRS, UMR 7242, ITI InnoVec, ESBS, 67412 Illkirch, France
[3] Faculté de Pharmacie, Université de Strasbourg, 67401 Illkirch, France
[4] Groupe Méthodes Recherche Clinique, Hôpitaux Universitaires de Strasbourg, 67000 Strasbourg, France
[5] Laboratoire iCube, UMR CNRS 7357, Equipe IMAGeS, Université de Strasbourg, 67000 Strasbourg, France
* Correspondence: julien.godet@unistra.fr
† Current address: Institut d'Optique & CNRS, LP2N UMR 5298, 33400 Talence, France.

Abstract: The pyoverdine siderophore is produced by *Pseudomonas aeruginosa* to access iron. Its synthesis involves the complex coordination of four nonribosomal peptide synthetases (NRPSs), which are responsible for assembling the pyoverdine peptide backbone. The precise cellular organization of these NRPSs and their mechanisms of interaction remain unclear. Here, we used a combination of several single-molecule microscopy techniques to elucidate the spatial arrangement of NRPSs within pyoverdine-producing cells. Our findings reveal that PvdL differs from the three other NRPSs in terms of localization and mobility patterns. PvdL is predominantly located in the inner membrane, while the others also explore the cytoplasmic compartment. Leveraging the power of multicolor single-molecule localization, we further reveal co-localization between PvdL and the other NRPSs, suggesting a pivotal role for PvdL in orchestrating the intricate biosynthetic pathway. Our observations strongly indicates that PvdL serves as a central orchestrator in the assembly of NRPSs involved in pyoverdine biosynthesis, assuming a critical regulatory function.

Keywords: *Pseudomonas aeruginosa*; NRPSs; pyoverdine; super-resolution microscopy; DNA-PAINT; co-localization; sptPALM; FLIM-FRET

Citation: Manko, H.; Steffan, T.; Gasser, V.; Mély, Y.; Schalk, I.; Godet, J. PvdL Orchestrates the Assembly of the Nonribosomal Peptide Synthetases Involved in Pyoverdine Biosynthesis in *Pseudomonas aeruginosa*. *Int. J. Mol. Sci.* **2024**, *25*, 6013. https://doi.org/10.3390/ijms25116013

Academic Editor: Ben Ovryn

Received: 10 April 2024
Revised: 20 May 2024
Accepted: 24 May 2024
Published: 30 May 2024

1. Introduction

Pseudomonas species exhibit remarkable adaptability to diverse environments associated with human activities due to their versatile metabolic capabilities [1]. Specific metabolic pathways can be activated in response to environmental conditions, enabling bacteria to generate a multitude of distinct secondary metabolites that confer fitness or selective advantages [2]. Non-ribosomal peptides (NRPs) are a large and diverse family of secondary metabolites that often serve specialized functions such as defense, communication, or colonization [3,4]. NRPs are synthesized by Non-Ribosomal Peptide Synthetases (NRPSs), a family of high-molecular-weight modular enzymes that can produce peptide molecules independently from ribosomes [5,6]. While ribosomal peptide synthesis is limited to 20 natural amino acids, NRPSs have the ability to use a diverse array of building blocks [7], enabling the synthesis of an extensive spectrum of secondary metabolites, encompassing toxins, virulence factors, and molecules with therapeutic interests [6]. In *P. aeruginosa*, the peptide backbone of pyoverdine is synthesized by four distinct NRPSs. Pyoverdine is the main siderophore produced by *P. aeruginosa* [8]. Siderophores are structurally diverse compounds with molecular weight ranging between 200 and 2000 Da, produced by pathogenic and nonpathogenic bacteria and fungi in order to access iron, a nutrient essential for cellular growth [9]. Owing to their capability to immobilize iron, siderophores can effectively

vampirize iron to deprive competing bacteria or the host of this essential nutrient [10]. Blocking the production of pyoverdine or using inhibitors has been reported as sufficient to mitigate *P. aeruginosa* pathogenesis [11,12]. Siderophores are also important mediators of interactions between members of microbial assemblies leading to cooperative, exploitative, and competitive interactions between individuals [13]. Pyoverdine is an example of a mediator for local mutualistic cooperation providing direct benefits to producers carrying the cost of production but also to non-producing but recipient cells [14]. Siderophores can also act as important mediators of interactions with eukaryotic hosts [15].

The pyoverdine biosynthesis process starts in the cytoplasm with the synthesis of a precursor of pyoverdine further maturated in the bacterial periplasm before secretion (Figure 1). In the cytoplasm, the synthesis involves a relatively intricate enzymatic system comprising four distinct NRPSs: PvdL, PvdI, PvdJ, and PvdD and three enzymes (PvdH, PvdA, and PvdF) producing modified amino acids. PvdL catalyzes the attachment of a fatty acid to a glutamate residue, followed by the addition of L-tyrosine and L-2,4-diaminobutyrate (L-Dab) to the product. The resulting three-amino-acid product is transferred to PvdI, which adds L-Serine, L-Arginine, L-Serine, and L-hydroxyornithine, and to PvdJ, which adds L-Lysine and L-Hydroxyornithine. Finally, PvdD adds two more L-Threonines and cyclizes the pyoverdine backbone [8,16]. Several attempts have been made to reveal the cellular organization of the enzymes involved in the pyoverdine biosynthesis pathway, leading to the suggestion that NRPSs may form a membrane-bound multi-enzymatic complex called the siderosomes [17–19]. Enzymes PvdH, PvdA and PvdF responsible for the biosynthesis of modified amino acids would also be part of the siderosomes. However, a clear bio-chemical characterization of siderosomes is missing. So far, they have not been isolated or reconstituted in vitro, which is possibly due to the large molecular weight of the NRPSs making them challenging to express and purify or simply because siderosomes form transiently in cells. These reasons might limit the investigation of siderosomes in their native environment. An in cellulo FRET-FLIM and single-molecule tracking revealed, for example, that the ornithine hydroxylase PvdA physically interacts with all four NRPSs, albeit with different stoichiometries depending on whether or not the NRPSs use the modified amino acids produced by PvdA [20].

Elaborate biosynthesis pathways, characterized by multiple sequential steps, have to be accurately regulated in order to effectively balance the competing imperatives of minimizing production costs while simultaneously optimizing reaction yields [8]. The regulation of these complexes is likely to involve the timely expression levels of the different enzymes, as well as their temporal stabilities and spatial organization. However, the spatial organization and dynamics of these four NRPSs in cells have received only minimal attention in the literature. More generally, data focusing on the spatial and temporal regulation of biosynthetic pathways in their native environment are scarce [21].

In this work, we propose to use a combination of single-molecule microscopy techniques to gain insight into the intracellular organization in cells of the four NRPSs of the pyoverdine biosynthesis pathway. We show that PvdL has a localization and mobility pattern distinct from the other three NRPSs. PvdL is mainly localized in the inner membrane while the others also explore the cytoplasmic compartment, thus having two diffusion regimes, one of which is very similar to that of PvdL. Leveraging the power of multicolor single-molecule localization microscopy, we further reveal co-localization between PvdL and the remaining NRPS. The unique localization and mobility patterns of PvdL suggest that it may play a key role in serving as an anchor point for other NRPSs during the dynamic process of pyoverdine biosynthesis.

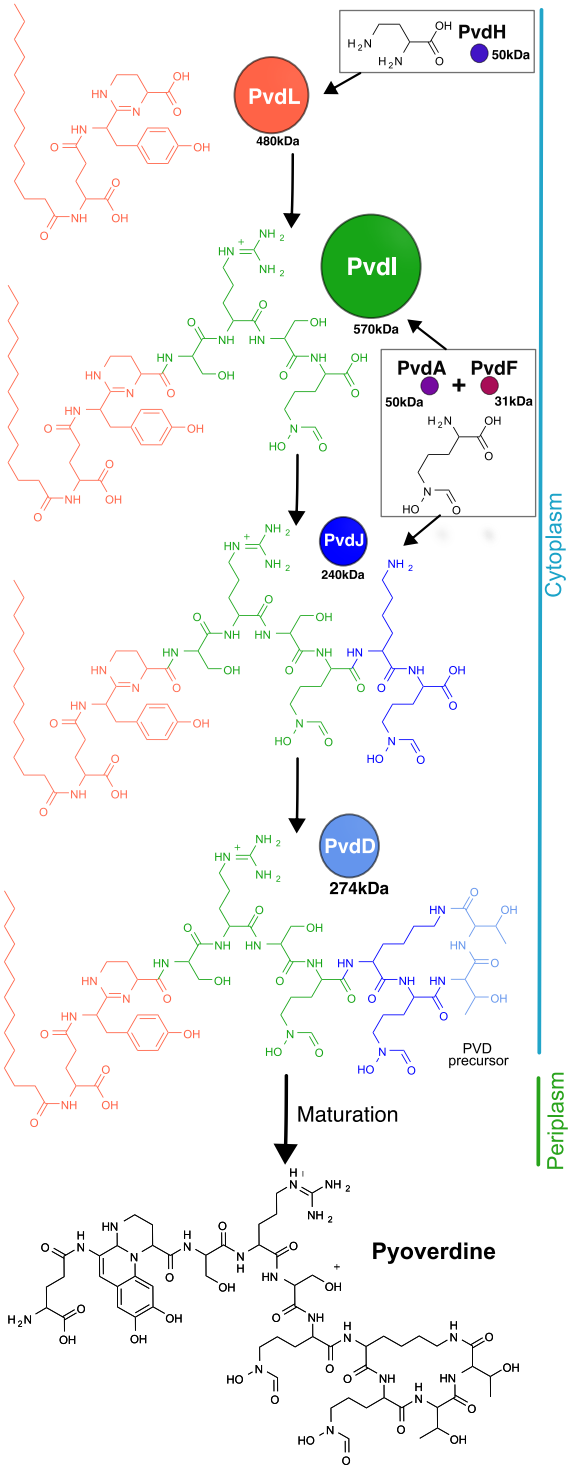

Figure 1. Assembly of the pyoverdine molecule. The cytoplasmic pyoverdine precursor is assembled by four NRPSs (PvdL, PvdI, PvdJ, and PvdD) with three smaller enzymes (PvdH, PvdA, and PvdF) providing modified amino acids. Every NRPS adds blocks (like amino acids) in the peptide backbone. In the very first step, PvdL introduces myristic acid, which is removed once the pyoverdine precursor is transported into the periplasm and before it undergoes maturation of the chromophore.

2. Results

2.1. Localizations of NRPSs in Cells

Bacteria have developed diverse mechanisms to address challenges associated with efficient growth and replication [22,23]. Precise regulation, including spatial control, of the

complex and resource-intensive metabolic pathways appears to be essential. Therefore, we sought to investigate the intracellular spatial localizations of the four NRPSs of the pyoverdine pathway using single-molecule localization DNA-paint microscopy.

We used *Pseudomonas aeruginosa* PAO1 strains in which either PvdL, PvdI, PvdJ, or PvdD was fused to eGFP at the chromosomal level. The expression of the fluorescent enzymes was induced by iron-deficient growing conditions similarly to the wild-type PAO1 [24]. In fixed cells, the eGFP moiety served as the target for immunostaining, where an anti-eGFP primary antibody was subsequently recognized by a secondary antibody containing a DNA-PAINT docking strand. In DNA-PAINT, the addition in the sample of short dye-labeled ('imager') oligonucleotides transiently binding to their complementary target ('docking') strands creates the necessary 'blinking' to enable stochastic single-molecule localization microscopy [25]. This approach offers several advantages compared to the direct imaging of labeled secondary antibodies, including the predictability of DNA binding and unbinding events, coupled with minimal (virtually zero) photo-bleaching [26]. This combination facilitates accurate NRPS localizations, as a single target protein is associated with multiple and repeatedly detectable fluorescence bursts within the sample.

Cell imaging was performed in three dimensions (3D) to reduce artefacts resulting from the two-dimensional projections of three-dimensional samples during 2D imaging. For the z-axis measurement, we used a cylindrical lens to introduce astigmatism into the imaging system. The z-encoded orientation of the PSF was then measured by fitting an ellipse to the image of the fluorophore. This approach allowed us to selectively build ~100 nm slices within the central portion of the bacteria and to compute a cross-sectional view (Figure 2). Interestingly, discrete punctate localizations along the cellular structure were observed for the four NRPSs. Cross-sectional observations revealed partial exclusion zones within the central region of the cell. This region probably corresponds to the area of the nucleoid (Figure 2a,b, cross-sectional views).

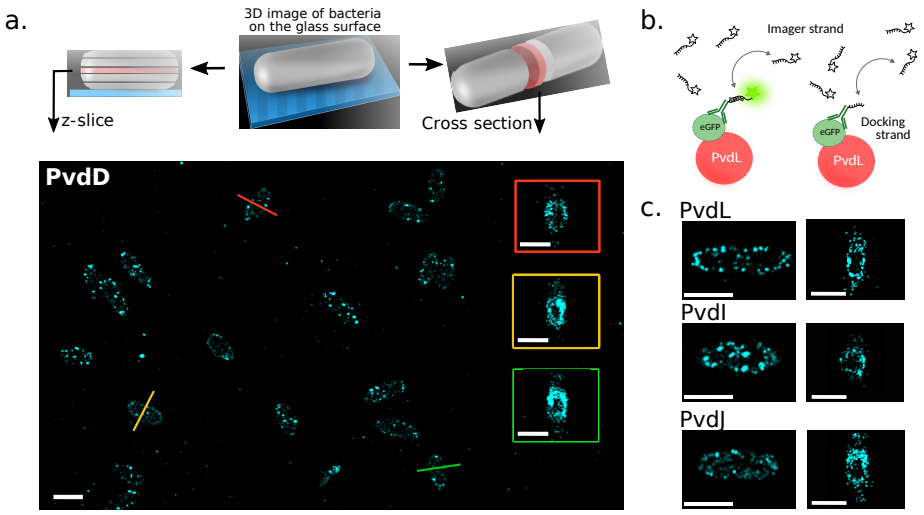

Figure 2. (**a**) Representative z-axis slice projections of 3D localizations of labeled PvdD in fixed bacterial cells on a glass coverslip (scale bar = 2 µm). Some cross-sections of bacteria are presented in the colored boxes (scale bar = 1 µm. (**b**) DNA-PAINT principle: DNA-PAINT uses DNA's specific interactions for super-resolution imaging. Fluorescently tagged DNA strands (imagers) briefly bind to target molecules tagged with complementary DNA (docking strand) to create the necessary 'blinking' for precise localization and high-resolution image reconstruction in single-molecule localization microscopy. (**c**) z-projections and cross-sections obtained for PvdL, PvdI, and PvdJ in fixed *P. aeruginosa* cells (scale bars = 1 µm).

Previous reports showed the exclusion of large proteins from the dense nucleoid region [27,28]. But a nucleoid exclusion has not been described before for proteins of the pyoverdine pathway, neither by FRAP [19] nor by 2D-sptPALM experiments [20]—probably because much smaller proteins were tracked. The discrete distribution of the NRPSs throughout the cell is an interesting finding. It can ensure that NRPSs are equitably distributed to the daughter cells during replication. It can also increase the surface area for interactions with other molecules or create local microenvironments that are conducive to pyoverdine production. Nevertheless, these data obtained with the DNA-PAINT technique were from paraformaldehyde-fixed bacteria. While we assume that neither fixation nor immunostaining perturbs the distribution of NRPSs in cells, it is important to note that it provides a static picture of the enzymes localization. To overcome this limit, we sought to examine the diffusion patterns of NRPSs in living cells.

2.2. Diffusion of NRPSs in Living Cells

To explore the diffusion of NRPSs in their native environment, we generated strains expressing either PvdL, PvdI, PvdJ, or PvdD fused to a photoactivatable mCherry (PAmCherry) at the chromosomal level. We performed single-particle tracking localization microscopy (sptPALM) [29] with high oblique illumination on living cells expressing the NRPS and immobilized on an agarose pad. The tracking data set was derived from a minimum of four independent experimental replicates. Once the localizations were determined frame-by-frame with sub-diffraction precision, the molecular trajectories were reconstructed based on the Linear Assignment Problem (LAP) tracker algorithm [30,31]. The trajectories were clustered by cell to create cellular diffusion maps (Figure 3a).

A comparison of the four representative diffusion maps (Figure 3a) indicates that the density of the trajectories differs between the different NRPSs in accordance with their relative expression in the cells—PvdL being the least expressed and PvdD being the most expressed. This visual impression was further reinforced by the fact that the areas explored by the trajectories were not the same. As represented by the jump size color code, PvdL diffusion was the most restricted (small jumps) with low-exploration traces remaining close to the cell boundary. On the contrary, PvdI, PvdJ, and PvdD showed different regimes of diffusion, with low-exploration traces at the outline of the cell coexisting with traces exploring a much larger surface inside the cell (Figure 3a). To provide further quantitative insight, we analyzed these data using jump distance analysis. Jump distance analysis calculates the distances between the positions of molecules in consecutive frames, each spanning a delta time corresponding to the time elapsed between the two frames (Δt = 40 ms) [32]. These distances are then plotted into a histogram to estimate a jump distance distribution. The jump distance distributions provide information about the diffusion coefficient of the molecules and facilitates the identification of distinct subpopulations of molecules diffusing at different rates in the sample (Figure 3b). In addition, we extended the analysis to different delta times (3, 4, 5 frames, and so forth) to investigate whether molecules were undergoing confined diffusion and to distinguish between extremely slow diffusion and immobility (Figure 3c). Varying the delta time allows the JD analysis to converge towards a mean square displacement (MSD) analysis but with the ability to estimate an MSD for each subpopulation of molecules.

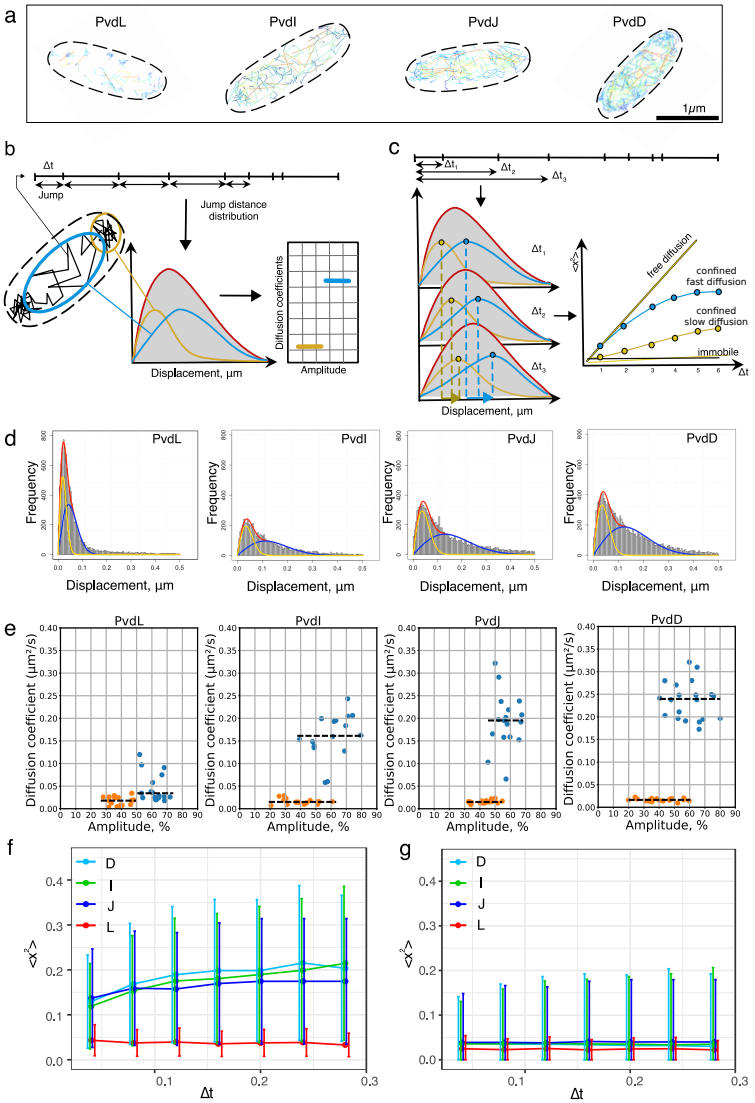

Figure 3. (**a**) Diffusion maps: Representative diffusion maps for PvdL, I, J, and D illustrate differences in the number of trajectories and explored surface areas. (**b**) Jump distances are computed from molecule trajectories using a fixed elapsed time. During a given time interval Δt, slowly diffusing molecules experience small jumps (orange), while faster diffusing molecules experience large jumps over the same time interval (blue). The jump distributions are estimated using a histogram from which the diffusion coefficients and the relative amplitude of the different diffusing subpopulations can be extracted. (**c**) Mean square displacement: By varying the time intervals, new jumps can be calculated, resulting in different distributions unless the molecules are immobile. The mean square displacement of the different subpopulations of diffusing molecules can be estimated to distinguish between free, confined, or immobile diffusion. (**d**) Experimental jump distance histograms corresponding to one field of view in the sample. The histograms were fitted using a two-component model, with fast (blue line) and slow (orange line) diffusion regimes. (**e**) Diffusion parameters: The diffusion coefficients and the corresponding amplitudes of the fast (blue dots) and the slow (orange dots) diffusion modes were determined. Each dot corresponds to the coefficient calculated by analyzing all the tracks containing more than three spots in one field of view. The median values of the diffusion coefficient are shown as black dashed lines. (**f**) Mean square displacement: MSD (median ± sd) as a function of Δt for the fast regimes of diffusion of the NRPSs. (**g**) Mean square displacement as a function of Δt for the slow regimes of diffusion of the NRPSs.

The best fits to describe the NRPS jump distance distributions were obtained for two-population models (Figure 3d). Interestingly, the values of the diffusion coefficients for the

slow diffusion mode were similar for all four NRPSs (see orange points in Figure 3e). The diffusion coefficients corresponding to the fast mode were found to be slightly different between PvdI, PvdJ, and PvdD and highly different from that of PvdL. The fast diffusion coefficients of PvdI, L, and D seemed to differ independently of their molecular weight (Figure 3e, blue points). The diffusion mode in the bacterial cytoplasm is difficult to interpret from the values of the diffusion coefficient, but it suggests that NRPSs could diffuse as complexes or multimers. The slowest diffusion rate was found for PvdL with a diffusion coefficient of 0.05 [0.02 to 0.06] $\mu m^2 s^{-1}$ (mean, [interquartile range (IQR)]) (Figure 3e, blue points). The diffusion coefficients of the two diffusion modes of PvdL were found to be close (Figure 2c), allowing the histogram to be fitted adequately with a single population in some cells. This suggests that PvdL is mostly confined to the inner membrane with a rare exploration of the cytoplasmic compartment.

Even when bound to the inner membrane, the diffusion of PvdL is slow. This was confirmed by the MSD curves corresponding to the slow component, which did not increase with increasing Δt (Figure 3g). This shows that a fraction of PvdL appeared immobile in the membrane when tracked with a pointing precision of about 30 nm. In line with the fact that the jump distribution could almost be considered a single population, the MSD of the faster component also remained constant over the Δt range (Figure 3f). On the contrary, PvdI, J, and D showed an MSD compatible with confined diffusion, as expected from the dimension of the cytoplasmic compartment in which these proteins can diffuse [33]. Interestingly and like PvdL, their slow component appeared to be immobile. Despite the limitations of the 2D projections, the locations of the immobile tracks suggest that slow diffusion regimes mostly occur near the inner membrane (see Supplementary Figure S1).

Taken together, these results suggest that PvdL behaves differently from the three other NRPSs. PvdL is almost exclusively associated with the inner membrane with very rare excursions into the cytoplasm. In contrast, PvdI, J, and L diffuse in the cytoplasm. They also experience a slow diffusion mode that is very similar to that of PvdL, suggesting that the different NRPSs assemble in a large complex in the inner membrane. Therefore, we sought to investigate direct NRPS-NRPS interaction in living cells.

2.3. NRPS-NRPS Interactions

To explore direct NRPS-NRPS interactions in living cells, we used Förster resonance energy transfer measured by fluorescence lifetime imaging (FLIM-FRET) [34]. FLIM-FRET allows for the measurement and the mapping of the fluorescence lifetime of a donor fluorophore directly in living cells. If FRET occurs, the fluorescence lifetime of the donor fluorophore decreases due to the non-radiative energy transfer to an acceptor fluorophore that is located in close proximity (typically in the range of 1 to 10 nm). The strong distance dependence of FRET ($\propto 1/R^6$) means that it is only possible for FRET to occur when the donor and acceptor fluorophores are located very close to each other (<10 nm). At the level of proteins, this almost always corresponds to situations where physical interactions occur. Therefore, FLIM-FRET is particularly suitable for measuring direct protein–protein interactions.

We used different combinations of protein mutants in which one NRPS was fused to eGFP (donor) and another to mCherry (acceptor) (Table 1). We also used bacteria expressing the appropriate NRPS tagged with eGFP only as control (donor only). In these combinations, PvdL was systematically one of the two NRPSs that was tagged with a fluorescent protein. The lifetime values of a donor alone (τ_d) and in the presence of an acceptor (τ_{da}) are shown in Table 1. The change in lifetime due to an acceptor was the most pronounced for the PvdL/PvdD pair. It was associated with a clear shift in the position of the lifetime phasor (Figure 4), confirming an interaction between the two proteins. The lifetime values did not change when the acceptor was present for the PvdL/PvdJ pair. The decrease in the donor lifetime in the PvdL/PvdI was limited, with a FRET efficiency almost indistinguishable from noise. Therefore, it was not possible to evidence FRET for an NRPS pair other than PvdL/PvdD. Nevertheless, due to the large size of NRPSs, these data cannot completely rule out the presence of direct interactions between these proteins, even in the absence of

FRET. Indeed, if the presence of FRET indicates interaction, the absence of FRET does not necessarily indicate an absence of interaction because the two fluorescent tags can fall too far apart in the complex. Ideally, NRPS labeling should be performed at positions other than the N- or C-termini to increase the likelihood of measuring FRET when proteins interact. However, without a structural understanding of potential interaction sites, internal labeling seemed arbitrary. There was also a risk of losing NRPS functionality. We, therefore, chose to investigate potential interactions between NRPSs using co-localization measurements.

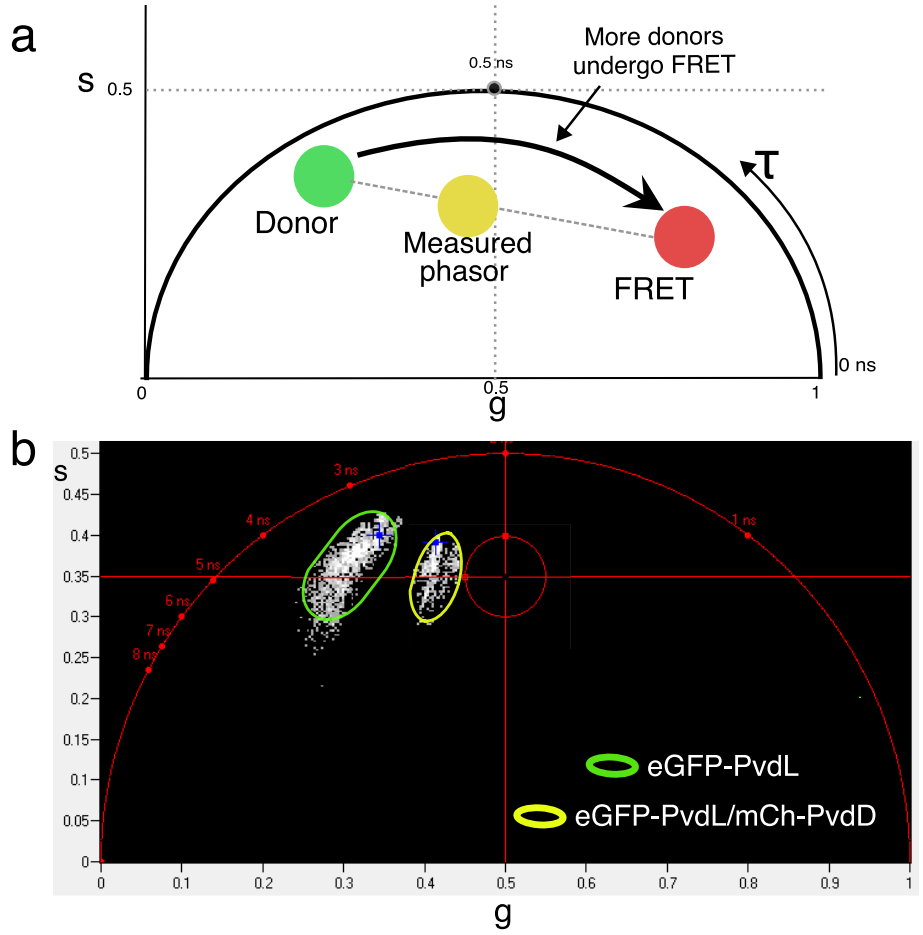

Figure 4. (**a**) Phasor approach principle. On a phasor plot, each phasor point is obtained by a transformation of the fluorescence decay of one FLIM pixel. The phasor coordinates are defined by real (g) and imaginary (s) parts of the Fourier transform. The position of the donor in the phasor plot will depend on its lifetime (green filled circle). When all the donor molecules undergo FRET with a high transfer efficiency, the phasor is shifted in the direction of lower lifetimes (red filled circle). In the case of a lower FRET efficiency, the phasor will stand on the line joining the two previously described positions (yellow filled circle). (**b**) Phasor plot. A clear shift between phasors of the donor (eGFP-PvdL, green oval) and the donor acceptor pair (eGFP-Pvdl/mCh-PvdD, yellow oval) can be seen, showing a protein–protein interaction between PvdL and PvdD.

Table 1. The average lifetime values for donors (τ_d), donor–acceptor pairs (τ_{da}), and FRET efficiency observed through FLIM-FRET experiments for PvdL and the three other NRPSs.

Strain Name	τ_d (ns)	τ_{da} (ns)	FRET Efficiency
eGFP-PvdL/PvdJ-mCherry	2.3	2.3	0.00
PvdJ-eGFP/mCherry-PvdL	2.3	2.3	0.00
eGFP-PvdL/mCherry-PvdD	2.3	2.0	0.13
eGFP-PvdL/PvdI-mCherry	2.3	2.2	0.04

2.4. Co-Localizations of NRPSs

For the co-localization experiments, we used the same *P. aeruginosa* double mutants as those used for the FLIM-FRET experiments, but we fixed and permeabilized the cells to allow for DNA-PAINT immunolabeling. We performed dual-color DNA-PAINT with imager strands labeled with Cy3B or Atto655, which specifically target docking strands attached to an anti-mouse secondary antibody targeting anti-eGFP antibody and to an anti-rabbit secondary antibody targeting anti-mCherry antibody, respectively. Samples were imaged for 60,000 frames with an exposure time of 80 ms per frame using focus drift control and alternating illumination sources every 20,000 frames. Localizations were extracted from raw images. When localizations were detected over several consecutive frames, the signals were merged into a single detection event. Retrieved localizations were then plotted with a false color according to their channels.

As shown in Figure 5a, the localizations observed in both channels coincided partially. To provide a quantitative measure of the co-localization, we calculated the Mander's overlap coefficients (MOCs) [35] directly from the localizations using an approach based on Voronoi diagrams [36]. The MOC is a measure of how much two signals co-occur spatially, indicating the extent to which they are localized in the same cellular or subcellular regions. It can range from 0 to 1, where 0 indicates no overlap and 1 indicates perfect overlap (Figure 5b). Two coefficients, M1 and M2, can be calculated. They represent the proportion of one signal that overlaps with the other signal, normalized by the total intensity of one of the two signals. The dissimilarities between the M1 and M2 values are informative about the asymmetry in the spread of co-localizations or may express differences in the level of expression of the proteins. Compared to pixel-by-pixel calculations, MOC calculated from localizations allows for a more robust determination because the position of fluorescent molecules is less likely to be affected by background noise than pixel intensity values. Mander's overlap coefficients [36] were calculated in multiple fields of view for each double mutant. For the eGFP-PvdL/PvdJ-mCherry pair, the median MOC was about 0.30 for M1 and M2, with the interquartile range ranging from 0.2 to 0.5 for M1 and 0.1 to 0.5 for M2. This indicates that a significant fraction of PvdL proteins (about one third) co-localized with PvdJ (Figure 5c). This is intriguing because no FRET could be seen between these two proteins. To confirm this observation, the same calculations were performed for the PvdJ-eGFP/mCherry-PvdL pair. Interestingly, the median MOCs were about 0.2 and 0.25, confirming that these two proteins co-localize (Figure 5c). In line with the direct interactions evidenced by FRET, the median M1 and M2 values for PvdL/PvdD were about 0.4. It indicates that about 40% of the signal of PvdL is co-localized with PvdD, and *vice versa*—fully consistent with the amplitude of the low diffusing species for both PvdL and PvdD (Figure 3e). More surprisingly, MOC values for PvdL/PvdI were even higher with both M1 and M2 about 0.6 (Figure 5c).

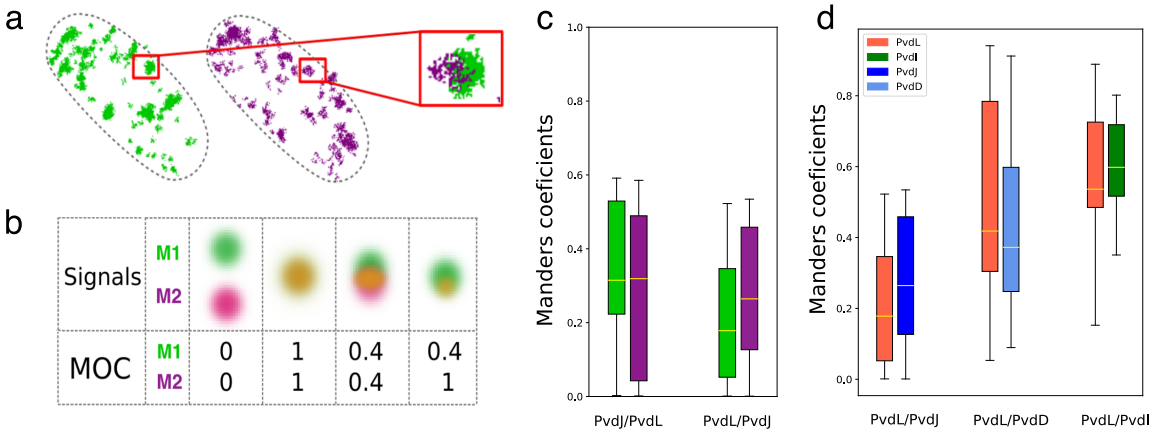

Figure 5. (**a**) Two-color localization microscopy Scatter plot of the localizations of single eGFP-PvdL (green) and PvdJ-mCherry (purple) in a cell showing partial co-localization of the two enzymes.

(**b**) Illustration of Mander's overlap coefficients. Mander's overlap coefficients show how much two fluorescent signals (M1 green and M2 purple, for example) in an image overlap. MOC indicates the area fraction of one signal localization that is also present in locations where the other channel is present. MOC ranges from 0 to 1. Asymmetric MOC values show how the spread and/or densities of co-localizations differ. (**c**) M1 and M2 Mander's overlap coefficients calculated for eGFP-PvdL/PvdJ-mCherry and PvdJ-eGFP/mCherry-PvdL. (**d**) Mander's overlap coefficients obtained for PvdL with the three other NRPSs. The highest values were obtained for the PvdL/PvdD and PvdL/PvdI pairs.

Taken together, PvdL partially co-localizes with all three NRPSs. This finding is in line with the similarity observed between the diffusion coefficients of the slowly diffusing subpopulations of each NRPS and those of PvdL. This strongly suggests that PvdL could have a significant role in coordinating NRPS assembly within the pyoverdine pathway, thus assuming a central regulatory function.

3. Discussion

In this work, we used a combination of several super-resolution microscopy techniques to study the organization of NRPSs in cells producing pyoverdine. We found that, in addition to the co-localization of subpopulations of PvdI, PvdJ, and PvdD with PvdL, all these enzymes share a common diffusion regimen with very low mobility. We also evidenced direct PvdD-PvdL interaction in live cells. These observations suggest the formation of complexes aggregating all the NRPSs involved in biosynthesis pathways of the cytoplasmic pyoverdine precursor, and that these complexes coexist with free NRPS fractions. The free fractions of PvdI, PvdJ, and PvdD mainly diffuse in the cytoplasm, whereas the free fraction of PvdL diffuses almost exclusively at the level of the inner membrane. This organization is fully compatible with the existence of transient siderosomes producing pyoverdine in cells [8,17,18].

Cellular reactions within metabolic pathways often occur in membrane-associated multi-enzyme complexes, not by free-floating enzymes [37]. The diffusion rate of PvdL strongly suggests the protein is associated with the membrane. Immobilized enzymatic engineering provided evidence that a spatially organized enzymatic complex yields kinetic benefits including preventing intermediate diffusion, improving product yield, and controlling the flux of metabolites [38]. The aggregation of different NRPSs by PvdL is expected to contribute to the improved efficiency and specificity of pyoverdine biosynthesis, potentially facilitating more efficient substrate channeling. The presence of a fatty acid chain introduced by PvdL at the beginning of the synthesis of pyoverdine may contribute to this process [39].

The question of how PvdL is associated with the inner membrane still needs to be addressed. Unlike some bacterial NRPSs, the PvdL sequence does not contain transmembrane domains [7]. PvdA, a tailoring enzyme involved in pyoverdine biosynthesis, could potentially function as an anchoring enzyme, tethering the enzymatic complex to the membrane, similar to some signaling proteins [40]. PvdA possesses a hydrophobic, inner-membrane-anchoring domain at its N-terminus, facilitating its association with the inner membrane [17,41]. In addition, PvdA has been demonstrated to interact with PvdL and the three other NRPSs in live cells with multiple PvdA molecules binding to the NRPSs [20]. NRPS membrane association likely serves functions such as enzyme protection, precursor coordination [42], and peptide export efficiency. In this work, we did not explore the interaction of PvdL with PvdE, an ABC transporter responsible for the export of the acylated ferribactin (the pyoverdine cytoplasmic precursor) into the periplasm [16]. It would be intriguing to determine whether membrane-associated proteins or accessory proteins could not only aid PvdL membrane localization but also facilitate peptide export.

PvdL appears to play a pivotal role by cornerstoning the organization of the siderosome, not only by anchoring it to specific sites in the cell but also by regulating its behavior in terms of diffusion. The advantage for a dynamic complex, with free protein fractions

exchanging with the complex, over a stable complex is not very apparent. However, advantages like sensitivity to changes in the environment to allow the cell to respond more quickly can be considered. Thus, this organization might be involved in regulation, as fine control of the expression of PvdL alone might be sufficient to disrupt the efficiency of the entire process. Interestingly, the gene for PvdL is located separately from the genes for the other NRPSs [43]. PvdL could then be subject to distinct regulatory mechanisms, allowing for more fine-tuned control of its expression, and PvdL's expression could be more sensitive to certain environmental cues or bacterial states. However, exploring this regulation is challenging because delta or deficient mutants for the pyoverdine biosynthesis disrupt the positive feedback stimulating the expression of the whole pathway. Indeed, the pyoverdine metabolic pathway is expressed in conditions where the iron level is low but also when ferri-pyoverdine is sensed by its uptake transporter FptA, leading to the release of the PvdS and PvdI sigma factors, both activating the transcription of the genes encoding the different enzymes involved in pyoverdine biosynthesis. Investigating this regulatory mechanism could deepen our understanding of how Pseudomonas bacteria selectively switch the acquisition of iron from the pyoverdine pathway to one of its multiple other iron uptake pathways in response to changes in environmental iron availability [10]. This last point could be an important factor in prioritizing the expression of certain uptake pathways in the context of antibiotics, which would be vectorized via iron acquisition pathways [44].

In summary, single-molecule observations have revealed that PvdL plays a pivotal role in orchestrating the assembly of NRPSs involved in pyoverdine biosynthesis, suggesting a central regulatory function that will be interesting to explore.

4. Materials and Methods

4.1. Bacteria Mutants, Cell Culture, and Labeling

The *Pseudomonas aeruginosa* strains used in this study are listed in the Supplementary Material (Table S1). Mutants construction was performed as described in detail in [24]. Oligonucleotides used for mutant constructions are listed in the Supplementary Material (Table S2). For imaging, cells were grown in lysogeny broth (LB) (L3152 Sigma Aldrich, Saint-Quentin-Fallavier, France) at 30 °C under 200 rpm orbital shaking for 24 h. The expression of the pyoverdine pathway was induced by changing the culture media for Succinate media (SM). The SM composition of this iron-deprived media was 6 g L^{-1} K_2HPO_4, 3 g L^{-1} KH_2PO_4, 1 g L^{-1} $[NH4]_2SO_4$, 0.2 g L^{-1} $MgSO_4$ $7H_2O$, and 4 g L^{-1} sodium succinate, with the pH adjusted to 7.0 by adding NaOH. Cells were grown for 24 h in SM before being diluted 10 times and grown for an additional 24 h in fresh SM. Before measurements, the density of cells was controlled by measuring the optical density (OD) at 600 nm. The bacteria were diluted to OD_{600nm} = 0.1 and grown for 2 additional hours to reach OD_{600nm} $\sim$ [0.4–0.5]. Finally, cells were immobilized on a 1% agarose pad and used for sptPALM and FLIM-FRET experiments.

For DNA-PAINT microscopy, the cells were additionally fixed with 4% formaldehyde (Sigma-Aldrich) in PBS and permeabilized with lysozyme. Targets (eGFP in single-color experiments and eGFP/mCherry in two-color) were labeled using a DNA-PAINT Massive-AB-2-Plex labeling kit (Massive Photonics, Muenchen, Germany) according to the manufacturer's protocol.

4.2. Microscopy and Analysis

SptPALM and DNA-PAINT experiments were performed on a home-built bespoke Olympus IX-81 (Olympus, Rungis, France) inverted optical microscope controlled by Micro-Manager software (version 1.4.2). The microscope was equipped with a 100× 1.4 NA oil-immersion objective (Olympus, Rungis, France) and with a z-drift control and auto-focus system (ZDC Olympus, Rungis, France). The illumination was provided by a 405 nm diode laser (Oxxius, Lannion, France), 561 nm CW diode laser (Oxxius, Lannion, France), and 638 nm diode pumped laser (Cobolt 08-01 series, Optoprim, Vanves, France) through the objective in epi-illumination or HILO illumination. The fluorescence emission

was collected through the same objective and sent to the camera using a dichroic mirror (Di03-R561-t1/Di 650-Di01-Semrock (AHF Analysentechnik, Tuebingen, Germany)). Before the signal was detected by a 512 × 512 pixels electron multiplied charged couple device (EMCCD) camera (ImageEM-(Hamamatsu Photonics, Shizuoka, Japan)) using an EM gain of 400, the fluorescence signal was filtered by a longpass filter (Lp02-568RU-25/645LP Edge Basic, Semrock (AHF Analysentechnik, Tuebingen, Germany)).

In sptPALM experiments, the sample was simultaneously illuminated by 561 nm and 405 nm lasers. The intensity of the 405 nm activation laser was adjusted by using a continuous density filter (Thorlabs SAS, Le Mesnil-le-roi, France). For tracking, traces were obtained using the TrackMate plugin [30] for Fiji (version 2.3.0). The tracking was performed using a simple LAP tracker with a max linking distance of 0.5 µm. The gap-closing max distance was set to 0.5 µm and gap-closing max frame gap was chosen to be 2. Further, the data were analyzed using TrackR package in R (version 1.0.0) as described in [20].

In the DNA-PAINT experiments, the 561 nm and 645 nm lasers were sequentially switched while acquiring 20,000 frames in each channel at an 80 ms exposure time. The molecular localizations were obtained using ThunderSTORM plugin [45] in Fiji. Then, the localization files were additionally filtered in SMAP [46] where groups of localizations featuring less than 10 events were discarded, and the localizations located only within the 100 nm z-slice in the middle part of the bacteria were kept. Further analysis was performed on a z-projection of the filtered data.

4.3. FLIM-FRET

Time-correlated single-photon counting FLIM measurements were performed on a home-made two-photon excitation scanning microscope based on an Olympus IX70 inverted microscope with an Olympus 60 × 1.2NA water immersion objective operating in a de-scanned fluorescence collection mode. Ti:Sapphire oscillator (Mai Tai DeepSee, (Micro-controle Spectra Physics, Evry France)-80 MHz repetition rate, ≈70 fs pulse width) at 10–20 mW was used for two-photon excitation at 930 nm. Emitted photons were collected through a 680 nm short-pass filter (F75-680, AHF Analysentechnik, Tuebingen, Germany) and a 525/50 nm band-pass filter (F37-516, AHF Analysentechnik, Tuebingen, Germany) and directed to a fiber-coupled avalanche photo-diode (SPCM-AQR-14-FC, Perkin Elmer, Waltham, MA, USA) connected to a time-correlated single-photon counting (TCSPC) module (SPC830, Becker & Hickl, Berlin, Germany). More details on the FLIM FRET setup are given in references [24,47]. The data analysis was performed using a commercial software (SPCImage, V8.1, Becker & Hickl, Berlin, Germany).

Supplementary Materials: The following supporting information can be downloaded at: https://www.mdpi.com/article/10.3390/ijms25116013/s1.

Author Contributions: Conceptualization, H.M. and J.G.; methodology, V.G., H.M. and J.G.; validation, J.G., I.S. and Y.M.; formal analysis, H.M. and J.G.; investigation, H.M. and J.G.; resources, T.S., V.G., J.G., I.S. and Y.M.; data curation, H.M., J.G.; writing—original draft preparation, H.M. and J.G.; writing—review and editing, all authors; visualization, H.M. and J.G.; supervision, J.G.; project administration, J.G.; funding acquisition, J.G., I.S. and Y.M. All authors have read and agreed to the published version of the manuscript.

Funding: This research was funded by the Interdisciplinary Thematic Institute (ITI) InnoVec (Innovative Vectorization of Biomolecules, IdEx, ANR-10-IDEX-0002).

Institutional Review Board Statement: Not applicable.

Informed Consent Statement: Not applicable.

Data Availability Statement: The original data presented in the study are openly available at https://doi.org/10.6084/m9.figshare.25119089.v1 (accessed on 29 May 2024).

Acknowledgments: H.M.'s PhD fellowship was supported by a governmental fellowship. Y.M. is grateful to the 'Institut Universitaire de France (IUF)' for its support and the additional research time

provided. We acknowledge the Imaging Center PIQ-QuESt (https://piq.unistra.fr/ (accessed on 12 March 2024)), a member of the national infrastructure France-Bioimaging supported by the French Research Agency (ANR-10-INBS-04).

Conflicts of Interest: The funders had no role in the study design, data collection and interpretation, or the decision to submit the work for publication. The authors declare no other competing financial interests.

Abbreviations

The following abbreviations are used in this manuscript:

NRPS	Nonribosomal peptide synthetase
FLIM-FRET	Förster resonance energy transfer measured by fluorescence lifetime imaging
IQR	Interquartile range
MSD	Mean square displacement
JD	Jump distance
OD	Optical density

References

1. Crone, S.; Vives-Flórez, M.; Kvich, L.; Saunders, A.M.; Malone, M.; Nicolaisen, M.H.; Martínez-García, E.; Rojas-Acosta, C.; Catalina Gomez-Puerto, M.; Calum, H.; et al. The environmental occurrence of *Pseudomonas aeruginosa*. *Apmis* **2020**, *128*, 220–231. [CrossRef]
2. Vining, L.C. Secondary metabolism, inventive evolution and biochemical diversity—A review. *Gene* **1992**, *115*, 135–140. [CrossRef]
3. Gross, H.; Loper, J.E. Genomics of secondary metabolite production by *Pseudomonas* spp. *Nat. Prod. Rep.* **2009**, *26*, 1408–1446. [CrossRef]
4. Dell, M.; Dunbar, K.L.; Hertweck, C. Ribosome-independent peptide biosynthesis: The challenge of a unifying nomenclature. *Nat. Prod. Rep.* **2021**, *39*, 453–459. [CrossRef] [PubMed]
5. Gulick, A.M. Nonribosomal peptide synthetase biosynthetic clusters of ESKAPE pathogens. *Nat. Prod. Rep.* **2017**, *34*, 981–1009. [CrossRef] [PubMed]
6. Süssmuth, R.D.; Mainz, A. Nonribosomal Peptyde Synthesis—Principles and Pprospects. *Angew. Chem.* **2017**, *56*, 3770–3821. [CrossRef] [PubMed]
7. Finking, R.; Marahiel, M.A. Biosynthesis of nonribosomal peptides. *Annu. Rev. Microbiol.* **2004**, *58*, 453–488. [CrossRef]
8. Schalk, I.J.; Rigouin, C.; Godet, J. An overview of siderophore biosynthesis among fluorescent Pseudomonads and new insights into their complex cellular organization. *Environ. Microbiol.* **2020**, *22*, 1447–1466. [CrossRef]
9. Loaces, I.; Ferrando, L.; Scavino, A.F. Dynamics, Diversity and Function of Endophytic Siderophore-Producing Bacteria in Rice. *Microb. Ecol.* **2011**, *61*, 606–618. [CrossRef]
10. Schalk, I.J.; Perraud, Q. *Pseudomonas aeruginosa* and its multiple strategies to access iron. *Environ. Microbiol.* **2023**, *25*, 811–831. [CrossRef]
11. Imperi, F.; Massai, F.; Facchini, M.; Frangipani, E.; Visaggio, D.; Leoni, L.; Bragonzi, A.; Visca, P. Repurposing the antimycotic drug flucytosine for suppression of *Pseudomonas aeruginosa* pathogenicity. *Proc. Natl. Acad. Sci. USA* **2013**, *110*, 7458–7463. [CrossRef] [PubMed]
12. Kirienko, D.R.; Kang, D.; Kirienko, N.V. Novel pyoverdine inhibitors mitigate *Pseudomonas aeruginosa* pathogenesis. *Front. Microbiol.* **2019**, *10*, 3317. [CrossRef] [PubMed]
13. Sexton, D.J.; Schuster, M. Nutrient limitation determines the fitness of cheaters in bacterial siderophore cooperation. *Nat. Commun.* **2017**, *8*, 230. [CrossRef] [PubMed]
14. Weigert, M.; Kümmerli, R. The physical boundaries of public goods cooperation between surface-attached bacterial cells. *Proc. R. Soc. B Biol. Sci.* **2017**, *284*, 20170631. [CrossRef] [PubMed]
15. Kramer, J.; Özkaya, Ö.; Kümmerli, R. Bacterial siderophores in community and host interactions. *Nat. Rev. Microbiol.* **2020**, *18*, 152–163. [CrossRef] [PubMed]
16. Ringel, M.T.; Brüser, T. The biosynthesis of pyoverdines. *Microb. Cell* **2018**, *5*, 424–437. [CrossRef] [PubMed]
17. Imperi, F.; Visca, P. Subcellular localization of the pyoverdine biogenesis machinery of *Pseudomonas aeruginosa*: A membrane-associated "siderosome". *FEBS Lett.* **2013**, *587*, 3387–3391. [CrossRef] [PubMed]
18. Gasser, V.; Guillon, L.; Cunrath, O.; Schalk, I.J. Cellular organization of siderophore biosynthesis in *Pseudomonas aeruginosa*: Evidence for siderosomes. *J. Inorg. Biochem.* **2015**, *148*, 27–34. [CrossRef]
19. Guillon, L.; Altenburger, S.; Graumann, P.L.; Schalk, I.J. Deciphering protein dynamics of the siderophore pyoverdine pathway in *Pseudomonas aeruginosa*. *PLoS ONE* **2013**, *8*, e79111. [CrossRef]

20. Gasser, V.; Malrieu, M.; Forster, A.; Mély, Y.; Schalk, I.J.; Godet, J. In cellulo FRET-FLIM and single molecule tracking reveal the supra-molecular organization of the pyoverdine bio-synthetic enzymes in *Pseudomonas aeruginosa*. *Q. Rev. Biophys.* **2020**, *53*, e1. [CrossRef]
21. Qiu, X.Y.; Xie, S.S.; Min, L.; Wu, X.M.; Zhu, L.Y.; Zhu, L. Spatial organization of enzymes to enhance synthetic pathways in microbial chassis: A systematic review. *Microb. Cell Factories* **2018**, *17*, 120. [CrossRef] [PubMed]
22. Llopis, P.M.; Jackson, A.F.; Sliusarenko, O.; Surovtsev, I.; Heinritz, J.; Emonet, T.; Jacobs-Wagner, C. Spatial organization of the flow of genetic information in bacteria. *Nature* **2010**, *466*, 77–81. [CrossRef]
23. Surovtsev, I.V.; Jacobs-Wagner, C. Subcellular Organization: A Critical Feature of Bacterial Cell Replication. *Cell* **2018**, *172*, 1271–1293. [CrossRef] [PubMed]
24. Manko, H.; Normant, V.; Perraud, Q.; Steffan, T.; Gasser, V.; Boutant, E.; Réal, É.; Schalk, I.J.; Mély, Y.; Godet, J. Flim-fret measurements of protein-protein interactions in live bacteria. *J. Vis. Exp.* **2020**, *2020*, 1–21. [CrossRef]
25. Jungmann, R.; Avendaño, M.S.; Woehrstein, J.B.; Dai, M.; Shih, W.M.; Yin, P. Multiplexed 3D cellular super-resolution imaging with DNA-PAINT and Exchange-PAINT. *Nat. Methods* **2014**, *11*, 313–318. [CrossRef]
26. Schnitzbauer, J.; Strauss, M.T.; Schlichthaerle, T.; Schueder, F.; Jungmann, R. Super-resolution microscopy with DNA-PAINT. *Nat. Protoc.* **2017**, *12*, 1198–1228. [CrossRef] [PubMed]
27. Neeli-Venkata, R.; Martikainen, A.; Gupta, A.; Gonçalves, N.; Fonseca, J.; Ribeiro, A.S. Robustness of the process of nucleoid exclusion of protein aggregates in *Escherichia coli*. *J. Bacteriol.* **2016**, *198*, 898–906. [CrossRef]
28. Bakshi, S.; Siryaporn, A.; Goulian, M.; Weisshaar, J.C. Superresolution imaging of ribosomes and RNA polymerase in live *Escherichia coli* cells. *Mol. Microbiol.* **2012**, *85*, 21–38. [CrossRef]
29. Manley, S.; Gillette, J.M.; Lippincott-Schwartz, J. Single-Particle Tracking Photoactivated Localization Microscopy for Mapping Single-Molecule Dynamics. In *Methods in Enzymology*; Elsevier: Amsterdam, The Netherlands, 2010; Volume 475, pp. 109–120. [CrossRef]
30. Tinevez, J.Y.; Perry, N.; Schindelin, J.; Hoopes, G.M.; Reynolds, G.D.; Laplantine, E.; Bednarek, S.Y.; Shorte, S.L.; Eliceiri, K.W. TrackMate: An open and extensible platform for single-particle tracking. *Methods* **2017**, *115*, 80–90. [CrossRef]
31. Ershov, D.; Phan, M.S.; Pylvänäinen, J.W.; Rigaud, S.U.; Le Blanc, L.; Charles-Orszag, A.; Conway, J.R.; Laine, R.F.; Roy, N.H.; Bonazzi, D.; et al. TrackMate 7: Integrating state-of-the-art segmentation algorithms into tracking pipelines. *Nat. Methods* **2022**, *19*, 829–832. [CrossRef]
32. Weimann, L.; Ganzinger, K.A.; McColl, J.; Irvine, K.L.; Davis, S.J.; Gay, N.J.; Bryant, C.E.; Klenerman, D. A Quantitative Comparison of Single-Dye Tracking Analysis Tools Using Monte Carlo Simulations. *PLoS ONE* **2013**, *8*, e64287. [CrossRef] [PubMed]
33. Rowland, D.J.; Tuson, H.H.; Biteen, J.S. Resolving Fast, Confined Diffusion in Bacteria with Image Correlation Spectroscopy. *Biophys. J.* **2016**, *110*, 2241–2251. [CrossRef] [PubMed]
34. Periasamy, A.; Day, R.N. Visualizing protein interactions in living cells using digitized GFP imaging and FRET microscopy. In *Methods in Cell Biology*; Elsevier: Amsterdam, The Netherlands, 1999; Volume 58, pp. 293–314. [CrossRef]
35. Manders, E.M.; Verbeek, F.J.; Aten, J.A. Measurement of co-localization of objects in dual-colour confocal images. *J. Microsc.* **1993**, *169*, 375–382. [CrossRef] [PubMed]
36. Levet, F.; Julien, G.; Galland, R.; Butler, C.; Beghin, A.; Chazeau, A.; Hoess, P.; Ries, J.; Giannone, G.; Sibarita, J.B. A tessellation-based colocalization analysis approach for single-molecule localization microscopy. *Nat. Commun.* **2019**, *10*, 2379. [CrossRef] [PubMed]
37. Conrado, R.J.; Varner, J.D.; DeLisa, M.P. Engineering the spatial organization of metabolic enzymes: Mimicking nature's synergy. *Curr. Opin. Biotechnol.* **2008**, *19*, 492–499. [CrossRef] [PubMed]
38. Kang, W.; Ma, T.; Liu, M.; Qu, J.; Liu, Z.; Zhang, H.; Shi, B.; Fu, S.; Ma, J.; Lai, L.T.F.; et al. Modular enzyme assembly for enhanced cascade biocatalysis and metabolic flux. *Nat. Commun.* **2019**, *10*, 4248. [CrossRef] [PubMed]
39. Hannauer, M.; Schäfer, M.; Hoegy, F.; Gizzi, P.; Wehrung, P.; Mislin, G.L.; Budzikiewicz, H.; Schalk, I.J. Biosynthesis of the pyoverdine siderophore of *Pseudomonas aeruginosa* involves precursors with a myristic or a myristoleic acid chain. *FEBS Lett.* **2012**, *586*, 96–101. [CrossRef] [PubMed]
40. Pawson, T.; Scott, J.D. Signaling through scaffold, anchoring, and adaptor proteins. *Science* **1997**, *278*, 2075–2080. [CrossRef]
41. Meneely, K.M.; Barr, E.W.; Bollinger, J.M.; Lamb, A.L. Kinetic mechanism of ornithine hydroxylase (PvdA) from *Pseudomonas aeruginosa*: Substrate triggering of O2 addition but not flavin reduction. *Biochemistry* **2009**, *48*, 4371–4376. [CrossRef]
42. Wheeldon, I.; Minteer, S.D.; Banta, S.; Barton, S.C.; Atanassov, P.; Sigman, M. Substrate channelling as an approach to cascade reactions. *Nat. Chem.* **2016**, *8*, 299–309. [CrossRef]
43. Winsor, G.L.; Griffiths, E.J.; Lo, R.; Dhillon, B.K.; Shay, J.A.; Brinkman, F.S. Enhanced annotations and features for comparing thousands of Pseudomonas genomes in the Pseudomonas genome database. *Nucleic Acids Res.* **2016**, *44*, D646–D653. [CrossRef] [PubMed]
44. Schalk, I.J. Siderophore–antibiotic conjugates: Exploiting iron uptake to deliver drugs into bacteria. *Clin. Microbiol. Infect.* **2018**, *24*, 801–802. [CrossRef] [PubMed]
45. Ovesný, M.; Křížek, P.; Borkovec, J.; Švindrych, Z.; Hagen, G.M. ThunderSTORM: A comprehensive ImageJ plug-in for PALM and STORM data analysis and super-resolution imaging. *Bioinformatics* **2014**, *30*, 2389–2390. [CrossRef] [PubMed]

46. Ries, J. SMAP: A modular super-resolution microscopy analysis platform for SMLM data. *Nat. Methods* **2020**, *17*, 870–872. [CrossRef]
47. Godet, J.; Mély, Y. Exploring protein-protein interactions with large differences in protein expression levels using FLIM-FRET. *Methods Appl. Fluoresc.* **2020**, *8*, 14007. [CrossRef]